





Dynamical phase transitions in periodically driven Bardeen-Cooper-Schrieffer systems

H. P. Ojeda Collado ^{1,*}, Gonzalo Usaj ^{2,3}, C. A. Balseiro,^{2,3} Damián H. Zanette ^{2,4} and José Lorenzana ^{1,†}

¹*ISC-CNR and Department of Physics, Sapienza University of Rome, Piazzale Aldo Moro 2, I-00185 Rome, Italy*

²*Centro Atómico Bariloche and Instituto Balseiro, Comisión Nacional de Energía Atómica (CNEA)–Universidad Nacional de Cuyo (UNCUYO), 8400 Bariloche, Argentina*

³*Instituto de Nanociencia y Nanotecnología (INN), Consejo Nacional de Investigaciones Científicas y Técnicas (CONICET)–CNEA, 8400 Bariloche, Argentina*

⁴*Consejo Nacional de Investigaciones Científicas y Técnicas (CONICET), Argentina*



(Received 27 October 2022; accepted 13 January 2023; published 7 April 2023)

We present a systematic study of the dynamical phase diagram of a periodically driven BCS system as a function of drive strength and frequency. Three different driving mechanisms are considered and compared: oscillating density of states, oscillating pairing interaction, and oscillating external pairing field. We identify the locus in parameter space of parametric resonances and four dynamical phases: Rabi-Higgs, gapless, synchronized Higgs, and time-crystal phases. We demonstrate that the main features of the phase diagram are quite robust to different driving protocols and discuss the order of the transitions. By mapping the BCS problem to a collection of nonlinear and interacting classical oscillators, we shed light on the origin of time-crystal phases and parametric resonances appearing for subgap excitations.

DOI: [10.1103/PhysRevResearch.5.023014](https://doi.org/10.1103/PhysRevResearch.5.023014)

I. INTRODUCTION

The manipulation of many-body systems by periodic drives, usually referred to as “Floquet engineering,” has become a powerful tool to control properties of materials [1–4]. Floquet engineering has benefited from the tremendous advances in laser technologies and the advent of highly controllable systems [5] like ultracold atomic gases in optical traps [6–8] or cavities [9–11], ion chains [12], and nuclear spins. Some experimental demonstrations include quantum control of magnetism [13], topology [14], electron-phonon interactions [15], and broken symmetry phases such as superconductivity [16,17].

Superconductors are also one of the most popular platforms for quantum technologies. Quantum devices require the manipulation of the out-of-equilibrium system for as long as possible without losing coherence because of coupling to the environment. Thus, in the past years a large effort has been made to improve materials and devices to increase the energy relaxation time and the coherent dynamics [18–20].

Superconducting and ultracold atomic superfluid condensates present a unique opportunity to study many-body Floquet effects [21–29]. Because of a gap in the excitation spectrum, these systems tend to have long relaxation times. In

addition, in weak coupling, the dynamics can be described by a mean-field-like Hamiltonian with effective all-to-all interactions. Both effects contribute to provide a large window of time where energy relaxation processes are suppressed and the out-of-equilibrium dynamics can be studied. Furthermore, all-to-all interacting systems have aroused interest in the context of mean-field time crystals [27,30–33].

Notwithstanding all this growing interest, Floquet engineering in superconducting or superfluid condensates has not been addressed until recently [21,23,24,27,34–40]. For periodically driven BCS systems, Rabi-Higgs oscillations [21], parametric resonances, and Floquet time-crystal phases [24,27] have been demonstrated by considering a periodic time-dependent pairing interaction $\lambda(t)$.

Despite this progress, several questions remain open. Different dynamical phases have been identified [21,23,24,36] and a partial dynamical phase diagram has been presented for the driven BCS system in Ref. [27]. On the other hand, the order of the transition has not been discussed. Also, so far studies have concentrated on a driving mechanism in which the interaction parameter λ is time dependent (λ driving). However, it is also possible to envisage that the density of states (DOS) could be time dependent (DOS driving).

Here we present a systematic study of the dynamical phase diagram of a driven BCS system including driving frequencies such that $\hbar\omega$ lies below and above the gap and a large range of drive amplitudes and both λ - and DOS-driving mechanisms. The DOS-driving protocol is relevant for ultracold-atom setups as well as in condensed-matter systems where the electrons can couple to an electromagnetic field in the terahertz regime. In addition, a systematic comparison of driving mechanisms allows to separate universal features from mechanism-dependent details.

*hector.pablo.ojedacollado@roma1.infn.it

†jose.lorenzana@cnr.it

We show that the phase diagram is, in general, surprisingly rich with at least four dynamical phases (Rabi-Higgs, gapless, synchronized Higgs, and time-crystal phases) ubiquitously appearing for both driving protocols. Dynamical phase transitions (DPTs) are analyzed in detail and we demonstrate the existence of first- and second-order-like phase transitions. We analyze the parametric resonances discovered before [27] and discuss their origin in the context of the mapping to a classical dynamical system. In order to clarify the essential ingredients leading to parametric resonances, we compare the phase diagram for λ and DOS driving with the one corresponding to an external pairing field (third driving mechanism). Also, to highlight the relevance of the many-body interactions in the emergence of parametric resonances, we compare these phase diagrams to the one obtained in the case that the self-consistency of the BCS order parameter is neglected.

The paper is organized as follows: Section II introduces the model and the methods used. Section III presents the dynamical phase diagrams. Section IV discusses the dynamics in each phase. Section V analyzes the order of the transitions. In Sec. VI we present the mapping to a classical system of nonlinear oscillators. Finally, in Sec. VII we present our conclusions.

II. PERIODICALLY DRIVEN BCS MODEL

A. The pseudospin model

We consider the following time-dependent BCS Hamiltonian written in terms of Anderson pseudospins [41]:

$$\hat{H}_{\text{BCS}} = -2 \sum_{\mathbf{k}} \xi_{\mathbf{k}}(t) \hat{S}_{\mathbf{k}}^z - \lambda(t) \sum_{\mathbf{k}, \mathbf{k}'} \hat{S}_{\mathbf{k}}^+ \hat{S}_{\mathbf{k}'}^- \quad (1)$$

Here, $\xi_{\mathbf{k}} = \varepsilon_{\mathbf{k}} - \mu$ measures the energy of the fermions ($\varepsilon_{\mathbf{k}}$) from the Fermi level μ and λ is the pairing interaction. Either $\xi_{\mathbf{k}}(t)$ or $\lambda(t)$ is taken as time dependent. In the first case, for a uniform rescaling of the fermionic band, we can consider the DOS itself, ν , to be time dependent (DOS driving) while the second case defines λ driving. More details of the protocols will be given in the next section.

The $\frac{1}{2}$ -pseudospin operators are given in terms of fermionic operators as

$$\begin{aligned} \hat{S}_{\mathbf{k}}^x &= \frac{1}{2}(\hat{c}_{\mathbf{k}\uparrow}^\dagger \hat{c}_{-\mathbf{k}\downarrow}^\dagger + \hat{c}_{-\mathbf{k}\downarrow} \hat{c}_{\mathbf{k}\uparrow}), \\ \hat{S}_{\mathbf{k}}^y &= \frac{1}{2i}(\hat{c}_{\mathbf{k}\uparrow}^\dagger \hat{c}_{-\mathbf{k}\downarrow}^\dagger - \hat{c}_{-\mathbf{k}\downarrow} \hat{c}_{\mathbf{k}\uparrow}), \\ \hat{S}_{\mathbf{k}}^z &= \frac{1}{2}(1 - \hat{c}_{\mathbf{k}\uparrow}^\dagger \hat{c}_{\mathbf{k}\uparrow} - \hat{c}_{-\mathbf{k}\downarrow}^\dagger \hat{c}_{-\mathbf{k}\downarrow}), \end{aligned} \quad (2)$$

and $\hat{c}_{\mathbf{k}\sigma}^\dagger$ ($\hat{c}_{\mathbf{k}\sigma}$) is the usual creation (annihilation) operator for fermions with momentum \mathbf{k} and spin σ . The operator $\hat{S}_{\mathbf{k}}^\pm \equiv \hat{S}_{\mathbf{k}}^x \pm i\hat{S}_{\mathbf{k}}^y$ creates or annihilates a Cooper pair $(\mathbf{k}, -\mathbf{k})$.

Due to the all-to-all interaction, assumed in the second term of Eq. (1), one can use a time-dependent mean-field treatment [42–54] which yields the *exact* dynamics in the thermodynamic limit. The BCS mean-field Hamiltonian can be written as

$$\hat{H}_{\text{MF}} = - \sum_{\mathbf{k}} \hat{S}_{\mathbf{k}} \cdot \mathbf{b}_{\mathbf{k}}, \quad (3)$$

where $\mathbf{b}_{\mathbf{k}}(t) = (2\Delta(t), 0, 2\xi_{\mathbf{k}})$ is the mean field acting on the $\frac{1}{2}$ -pseudospin operator $\hat{S}_{\mathbf{k}} = (\hat{S}_{\mathbf{k}}^x, \hat{S}_{\mathbf{k}}^y, \hat{S}_{\mathbf{k}}^z)$. The

pseudomagnetic field $\mathbf{b}_{\mathbf{k}}$ has to be obtained in a self-consistent manner during the dynamics.

Without loss of generality, we consider that the equilibrium superconducting order parameter Δ_0 is real. We will assume this remains valid over time and show below that this is indeed the case because of the electron-hole symmetry.

The real part of the instantaneous BCS order parameter is given by

$$\Delta(t) = \lambda(t) \sum_{\mathbf{k}} S_{\mathbf{k}}^x, \quad (4)$$

where $S_{\mathbf{k}}^x$, without hat, denotes the expectation value of the operator $\hat{S}_{\mathbf{k}}^x$ in the time-dependent BCS state. From here on, we will use this notation for all pseudospin components.

In practice, since the pseudomagnetic field depends on \mathbf{k} only through $\xi_{\mathbf{k}}$, rather than solving the equations for each \mathbf{k} we solve the equations for a generic DOS converting the sums into integrals over the fermionic energy ξ ,

$$\Delta(t) = \lambda(t) \int d\xi \nu(\xi) S^x(\xi), \quad (5)$$

with $S^x(\xi_{\mathbf{k}}) \equiv S_{\mathbf{k}}^x$ and similar for the other components—we use $S_{\mathbf{k}}^x$ and $S^x(\xi_{\mathbf{k}})$ interchangeably, keeping in mind that in actual computations the ξ -dependent form was used.

At equilibrium, in the absence of periodic perturbations, the $\frac{1}{2}$ -pseudospins align in the direction of their local fields $\mathbf{b}_{\mathbf{k}}^0 = (2\Delta_0, 0, 2\xi_{\mathbf{k}})$ in order to minimize the system's energy [described by Eq. (3)]. This corresponds to the zero-temperature paired ground state in which the pseudospin texture (the expectation value of pseudospin operators as a function of momentum \mathbf{k}) is given by

$$S_{\mathbf{k}}^{x,0} = \frac{\Delta_0}{2\sqrt{\xi_{\mathbf{k}}^2 + \Delta_0^2}}, \quad S_{\mathbf{k}}^{y,0} = 0, \quad S_{\mathbf{k}}^{z,0} = \frac{\xi_{\mathbf{k}}}{2\sqrt{\xi_{\mathbf{k}}^2 + \Delta_0^2}}. \quad (6)$$

Such pseudospin texture is used as an initial condition and, once the pairing interaction or the DOS is modulated in time, the expectation values of the pseudospins evolve obeying a Bloch-like equation of motion,

$$\frac{d\mathbf{S}_{\mathbf{k}}}{dt} = -\mathbf{b}_{\mathbf{k}}(t) \times \mathbf{S}_{\mathbf{k}}, \quad (7)$$

where we set $\hbar \equiv 1$.

We assume that the time-dependent solutions do not spontaneously break particle-hole symmetry. From the equations of motion one can check that if $b^y(\xi) = \Delta'' = 0$ (with Δ'' the imaginary part of the order parameter) then since $b^x(\xi) = b^x(-\xi) = 2\Delta$ and $b^z(\xi) = b^z(-\xi)$ the self-consistent solution preserves the following symmetries:

$$\begin{aligned} S^x(\xi) &= S^x(-\xi), \\ S^y(\xi) &= -S^y(-\xi), \\ S^z(\xi) &= -S^z(-\xi). \end{aligned} \quad (8)$$

Indeed, the imaginary part of the order parameter is given by

$$\Delta''(t) = \lambda(t) \int d\xi \nu(\xi) S^y(\xi), \quad (9)$$

which vanishes if Eq. (8) holds [and $v(\xi) = v(-\xi)$ as assumed]. Now, by considering Δ'' at a time $t + dt$,

$$\begin{aligned} \Delta''(t + dt) - \Delta''(t) &= dt\lambda(t) \int d\xi v(\xi)[b^x(\xi)S^z(\xi) - b^z(\xi)S^x(\xi)] \\ &= 0. \end{aligned} \quad (10)$$

This shows that the $\Delta''(t) = 0$ is preserved at all times. Thus, our initial assumption and also Eqs. (8) are self-consistently satisfied at all times.

B. Numerical implementation

In our computations, we consider typically $N = 10^4$ pseudospins associated to equally spaced discrete energy states ξ_k within an energy range of $W = 40\Delta_0$ around μ with an energy constant density of states, v . The N coupled differential equations arising from Eq. (7) are solved using a standard Runge-Kutta fourth-order method with a small enough dt ensuring the convergence of dynamics. Some selected points in the phase diagram were also checked using an adaptive step-size Runge-Kutta method (Fehlberg method).

C. Driving protocols

In the following, we consider two different driving protocols. In the λ -driving case, the pairing interaction is taken periodic in time, as

$$\lambda(t) = \lambda_0 [1 + \alpha \sin(\omega_d t)], \quad (11)$$

while ξ_k does not depend on time. Here, λ_0 is the equilibrium coupling constant, α is the driving strength, and ω_d is the drive frequency.

In DOS driving, we consider a time-periodic DOS with a time-independent pairing interaction λ_0 . This can be achieved with a periodic modulation of the Fermi velocity which corresponds to a change in the band structure as

$$\xi_k(t) = \xi_k^0 [1 + \beta \sin(\omega_d t)], \quad (12)$$

yielding a time-dependent DOS given by

$$v(t) = \frac{v_0}{1 + \beta \sin(\omega_d t)}, \quad (13)$$

where v_0 is the constant DOS at equilibrium. The equilibrium T_c and order parameter depend on the product λv so an adiabatic change in either parameter is equivalent. In contrast, the two protocols are rather different when the system is out of equilibrium and produce different dynamics. DOS driving implies that there is a momentum- and time-dependent pseudomagnetic field along z [through $\xi_k(t)$] which acquires x components once Δ becomes time dependent. On the other hand, λ drive means a time-dependent pseudomagnetic field only along the x direction. Possible experimental implementations of both protocols in ultracold atoms and condensed-matter systems have been discussed in detail in Ref. [21].

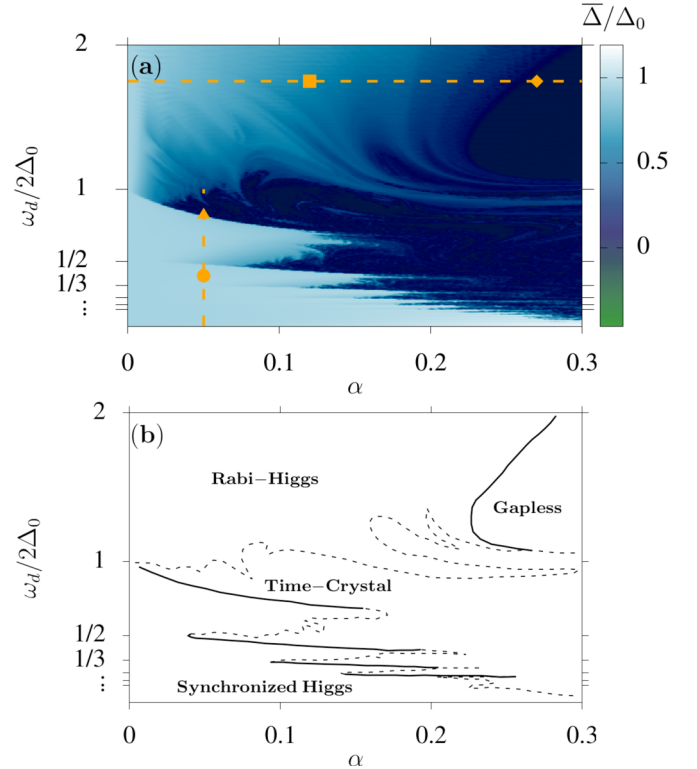


FIG. 1. (a) Temporal average of superconducting order parameter $\bar{\Delta}$ as a function of amplitude and frequency of the drive, considering a λ -driving protocol. We have computed $\bar{\Delta}$ using the time window $t\Delta_0 \in [0, 200]$. Dashed orange lines indicate cuts to be shown later (see Figs. 10 and 11). The orange dots indicate the parameters where the detailed dynamics is displayed (Fig. 2). They correspond to the different dynamical phases found: synchronized Higgs (circle), time crystal (triangle), Rabi-Higgs (square), and gapless (rhombus). (b) Schematic representation of the phase diagram showing the dominant phases in each region. Dashed curves represent continuous phase transitions with fractal-like boundaries while solid lines represent first-order DPTs as shown below.

III. DYNAMICAL PHASE DIAGRAMS

In this section, we present the dynamical phase diagram with both driving methods and in a wide range of frequency and driving strengths. Previous studies focused on λ driving and the subgap regime [27] or specific frequencies [21,23].

A first screening of the phase diagram can be obtained [27] using the time-averaged superconducting order parameter $\bar{\Delta}$ as a dynamical order parameter. In Fig. 1 we show a false color map of $\bar{\Delta}$ as a function of the amplitude and frequency of the drive for the λ -driving protocol. At first look, there are two main regions that can be easily distinguished: in the light blue regions the average of the superconducting order parameter is near the equilibrium value ($\bar{\Delta} \approx \Delta_0$) while regions with zero order parameter average (ZOPA) appear in dark blue. We identify four different dynamical phases within these regions, which are schematized and labeled in Fig. 1(b). However, these need a more refined analysis to be distinguished, as explained below.

Two dynamical phases appear for subgap excitations, and two when the system is driven above the gap $\omega_d > 2\Delta_0$. This

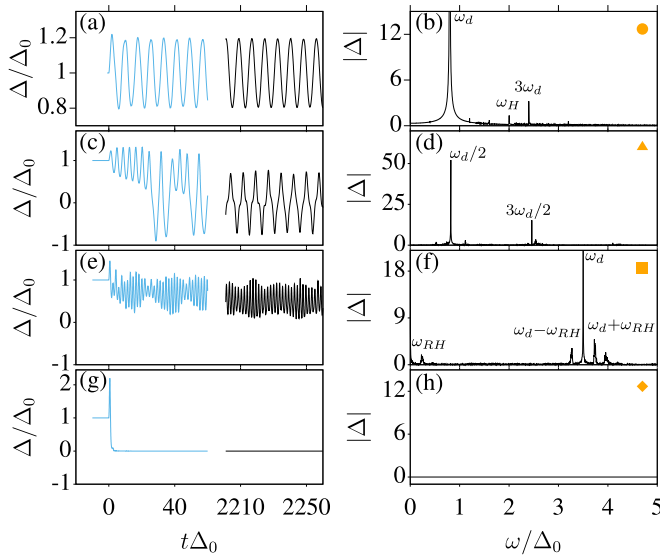


FIG. 2. Representative dynamical phases for the highlighted parameters (solid dots) of Fig. 1(a). In the left column we show the dynamics (transient in blue and steady state in black) and the FT in the corresponding right panel. For the Fourier analysis, we consider a long time window $t\Delta_0 \in [200, 2500]$ to obtain better resolution. [(a), (b)] Synchronized Higgs mode phase in which the system responds with the Higgs frequency $\omega_H = 2\bar{\Delta}$. [(c), (d)] Time-crystal phase as a consequence of a time-translational symmetry breaking in which the order parameter shows period-doubling oscillations. [(e), (f)] Rabi-Higgs mode phase, in which the superconducting order parameter oscillates with a low fundamental frequency ω_{RH} . Also in this regime, the Higgs mode ω_H appears as a very low peak in the FT which is not appreciable in the present scale but in the logarithmic scale used in Fig. 10. [(g), (h)] Gapless regime where $\Delta(t)$ goes very rapidly to zero and remains zero over time without exhibiting appreciable oscillations.

rather strong distinction could be anticipated as in one case it is not possible to directly excite quasiparticles in the system (for subgap excitations in an off-resonant regime) while for $\omega_d > 2\Delta_0$ it is possible.

For $\omega_d < 2\Delta_0$, dark indentations or “Arnold tongues” appear at $\omega_d = 2\Delta_0/n$, with n a natural number. These are the parametric resonances reported in Ref. [27]. The phase outside the Arnold tongues, labeled “synchronized Higgs,” is characterized by an order parameter quite close to equilibrium (light blue regions). In contrast, for $\omega_d > 2\Delta_0$ the non-ZOPA phases are characterized by a smaller average order parameter. Indeed, the light blue regions are darker when $\omega_d > 2\Delta_0$ than in the opposite case, indicating more quasiparticle excitations in the steady state.

In some regions the phase diagram has a marbled aspect indicating that, in general, different dynamical phases intermix. However, regions with predominance of a given phase can be identified as schematized in the lower panel.

An example of the time evolution and its Fourier transform (FT) for each one of the dynamical phases is shown in Fig. 2. The orange dots allow to associate the parameters of each row with their location in the phase diagram.

In the presence of a bath [23,36] the system can reach thermodynamic equilibrium and linear-response theory can be

applied. In the linear regime [21,55,56] the time-dependent gap parameter responds with the same frequency of the drive, so the time-translation-symmetry properties of the drive are preserved. Here, without a bath, for all four dynamical phases, this time-translation-symmetry preservation does not hold, so these are exquisitely nonlinear effects which can occur as prethermal phenomena [27].

In the synchronized Higgs phase, illustrated in Figs. 2(a) and 2(b), the superconducting order parameter oscillates not only with the drive frequency ω_d (and high harmonics) but also with a different and incommensurate fundamental frequency given by $\omega_H = 2\bar{\Delta}$ (fundamental Higgs frequency). In the time-crystal phase [Figs. 2(c) and 2(d)], after a transient dynamics, period-doubling oscillations are stabilized, indicating a subharmonic response. This is the typical behavior of discrete time-translational-symmetry breaking displayed by Floquet time crystals [32,57–63]. Notice that the drive frequency ω_d does not appear in the FT but the subharmonic response remains locked at $\omega_d/2$. This behavior persists under changes in the drive amplitude or frequency [27] which is the hallmark of time-crystal behavior [32,58].

For $\omega_d > 2\Delta_0$ and relatively small perturbation amplitudes α , the dynamics shows a slow modulation amplitude on top of the fast oscillations at frequency ω_d [see Fig. 2(e)]. This low-frequency mode has been denoted as ω_{RH} in the FT [Fig. 2(f)] and corresponds to the Rabi-Higgs mode reported in Ref. [21]. In this regime, a subset of pseudospins gets synchronized and performs Rabi oscillations with a frequency proportional to the amplitude of the drive. This corresponds again to a time-translation-symmetry-breaking subharmonic response. However, the frequency of the mode can be tuned with the external drive, which means that the response lacks “rigidity” and therefore does not qualify as a time-crystal phase according to the standard definitions [32,58].

Finally, by exciting above the gap with large drive amplitude, the system enters into a gapless regime in which the superconducting order parameter goes to zero very rapidly in time and then remains constant [Fig. 2(g)]. As we demonstrate in the following, the fact that $\Delta(t) = 0$ does not mean the absence of pairing in the system but a “perfect” dephasing between quasiparticles. Also in this case the response does not have the same periodicity of the drive. However, instead of symmetry breaking in this case there is symmetry restoring (since the response is more symmetric in time) although in a rather trivial way.

The real time evolution shows that for all dynamical phases there are lapses of time in which the superconducting order parameter is larger than the equilibrium value Δ_0 . This is more evident for the gapless regime [Fig. 2(g)] in which $\Delta(t)$ surpasses $2\Delta_0$ at very short times before getting down to zero. However, this value is still below the increase we could expect by considering an adiabatic evolution [53] where we use the instantaneous DOS or pairing interaction in the equilibrium gap equation. So this effect is rather trivial and should not be confused with dynamically induced superconductivity.

We present the same phase diagram [Fig. 3(a)] and the corresponding sketch [Fig. 3(b)] but now by considering the DOS-driving protocol. There are many common characteristics by comparing with Fig. 1. In particular, one sees that parametric resonances for $\omega_d < 2\Delta_0$ are robust features that

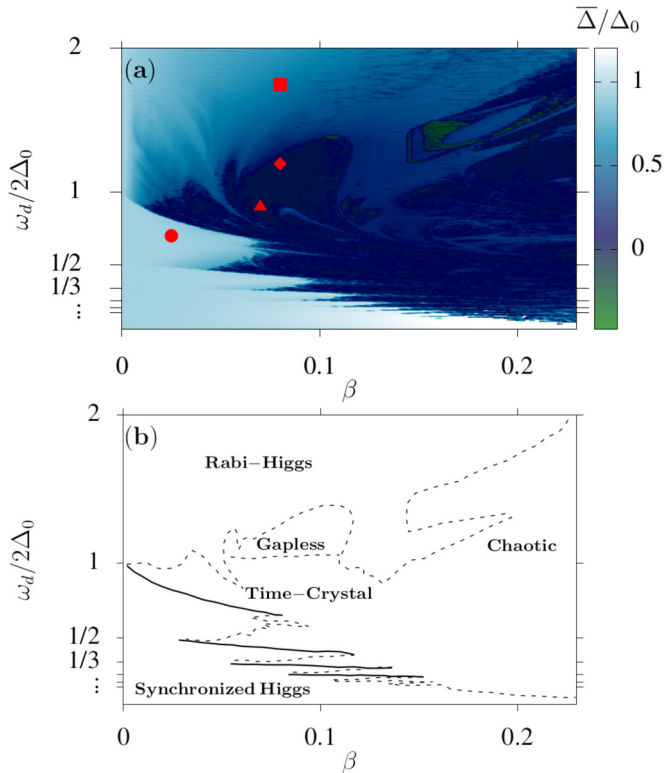


FIG. 3. (a) Temporal average of superconducting order parameter $\bar{\Delta}$ as a function of amplitude and frequency of the drive considering a DOS-driving protocol. We have computed $\bar{\Delta}$ using the time window $t\Delta_0 \in [0, 200]$. The red dots indicate the parameters used to illustrate the more prominent dynamical phases appearing in the phase diagram: synchronized Higgs phase (circle), time-crystal phase (triangle), Rabi-Higgs phase (square), and gapless phase (rhombus) (see Fig. 4). (b) Schematic representation of the phase diagram showing the dominant phases in each region. Dashed curves represent continuous phase transitions with fractal-like boundaries while solid lines represent first-order DPTs. In the rightmost part of the phase diagram, dynamical phases intermix in very small regions, forming a chaotic structure.

naturally emerge independently of the protocol details. Indeed, they appear both for periodic drive acting only along the pseudomagnetic field x direction (λ driving) or acting along the x and z axes at the same time (DOS-driving case). On the other hand, we show that the same dynamical phases appear with some difference in the details of the regions of stability. In contrast to the phase diagram for the λ -driving case, here, for large perturbation amplitudes ($\beta \gtrsim 0.15$), the dynamical phase diagram becomes more chaotic where all dynamical phases practically coexist in small regions.

For completeness, we show the different dynamics at the red points in Fig. 4.

The crucial role of interactions

The classical parametric oscillator with one degree of freedom [64] is the simplest mechanical system to show a subharmonic response, a key ingredient of time-crystal behavior. However, time crystals are defined also by their many-body

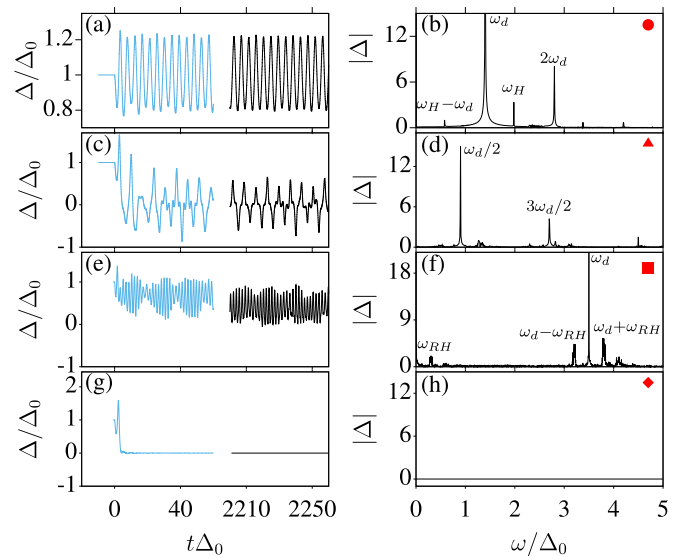


FIG. 4. The same as Fig. 2 for the parameters indicated in Fig. 3(a).

nature. Thus, a successful way to build time crystals is by making several parametric oscillators interact [65,66].

The dynamics of a single pseudospin in an external magnetic field is governed by Bloch equations, which can describe nontrivial phenomena such as Rabi oscillations. In analogy with the above systems, one can wonder if the subharmonic response is already built before interactions are switched on. To check for this, we solve the equation of motion (EOM) [Eq. (7)] with a non-self-consistent pseudomagnetic field,

$$\mathbf{b}_k(t) = 2(\Delta_0[1 + \alpha \sin(\omega_d t)], 0, \xi_k), \quad (14)$$

starting with the equilibrium initial condition [pseudospins texture of Eq. (6)].

In this case, the phase diagram becomes trivial without any visible Arnold tongues as shown in Fig. 5 where we report a false color plot of the temporal average of the order parameter, defined here as

$$\bar{\Delta} = \lambda_0 \sum_k \bar{S}_k^x. \quad (15)$$

It shows that differently from Refs. [65,66] the subharmonic response is not built in the elementary constituents but it is an emergent phenomenon which appears only after fully taking into account the quasiparticle interactions in the system. We will come back to this problem in Sec. VI where we will show how the system can be mapped to a collection of highly nonlinear oscillators.

IV. TYPICAL PSEUDOSPIN TRAJECTORIES FOR EACH DYNAMICAL PHASE

A more refined characterization of the dynamical phases can be obtained by studying the response resolved for each individual pseudospin. Here we show results for the λ -driving case but DOS driving yields similar results.

In some cases, the dynamics is more easily analyzed in terms of longitudinal and transverse components with respect to the direction of each pseudospin at equilibrium

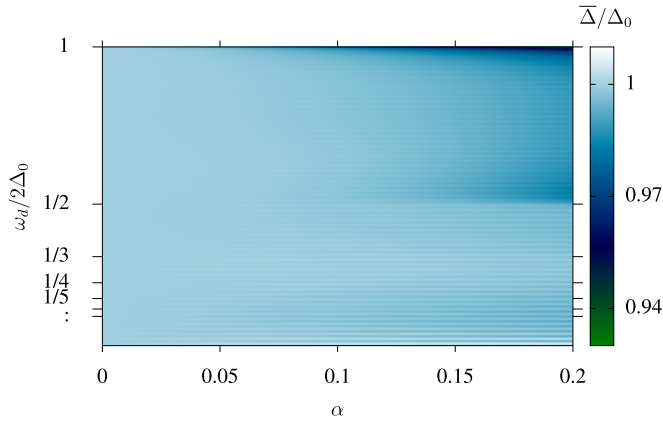


FIG. 5. Dynamical phase diagram for noninteracting pseudospins. We show the temporal average of the superconducting order parameter in the $\alpha - \omega_d$ plane for *noninteracting* pseudospins subject to an oscillating (non-self-consistent) pseudomagnetic field. In this case, parametric resonances are absent and only a weak feature appears for subgap excitation at $\omega_d \approx \Delta_0$ and large driving amplitude. This feature becomes visible by zooming the intensity scale to a small window around Δ_0 (notice the different color bar scale with respect to the other figures).

(i.e., without drive). Thus, we define a pseudospin-dependent reference frame, hereafter the equilibrium Larmor frame (ELF), introducing the unit vector along the equilibrium direction,

$$\hat{e}_k^\parallel = 2\mathbf{S}_k^0 = \frac{2}{\omega_k}(\Delta_0, 0, \xi_k), \quad (16)$$

and two transverse directions,

$$\hat{y} = (0, 1, 0), \quad (17)$$

$$\hat{e}_k^\perp = \hat{y} \times \hat{e}_k^\parallel = \frac{2}{\omega_k}(\xi_k, 0, -\Delta_0). \quad (18)$$

With these definitions the pseudospin deviations from equilibrium, $\delta\mathbf{S}_k \equiv \mathbf{S}_k - \mathbf{S}_k^0$, can be decomposed in longitudinal (\parallel) and transverse (\perp, y) components:

$$\delta\mathbf{S}_k = \delta S_k^\parallel \hat{e}_k^\parallel + \delta S_k^\perp \hat{e}_k^\perp + \delta S_k^y \hat{y}. \quad (19)$$

Notice that since the pseudospins are normalized to length $1/2$, giving two components specifies the vector up to a sign of the third component.

A. Synchronized Higgs phase

Figure 6 shows snapshots of the steady-state dynamics for the synchronized Higgs phase in the ELF during a driving period, $T_d = 2\pi/\omega_d$. The color encodes the fermionic energy ξ_k . Notice that because of particle-hole symmetry [Eqs. (8)] it is enough to show the pseudospins for $\xi_k > 0$ to specify the full texture. In this dynamical phase, the pseudospins precess very close to their equilibrium position represented by the origin. Pseudospins with quasiparticle energy $\xi_k \simeq \Delta_0$ (purple dots) oscillate with the drive frequency in such a way that they perform a full anticlockwise turn in a drive period T_d . In contrast, the low-energy pseudospins (black dots) precess more rapidly, so that by $t = 3T_d/8$ they have performed more than a full turn. Their frequency $2\bar{\Delta}$ corresponds to the Higgs mode. Notice that the loop shape formed by the low-energy pseudospins (in black) preserves its form during the evolution, indicating that there is no significant dephasing. Indeed, synchronization of these pseudospins yields the main contribution to the Higgs mode. Because of particle-hole symmetry, the pseudospin at the Fermi level cannot be excited by the drive. In general one can show that the deviation from the equilibrium position should decrease for low-energy pseudospins (black dots) as indeed observed.

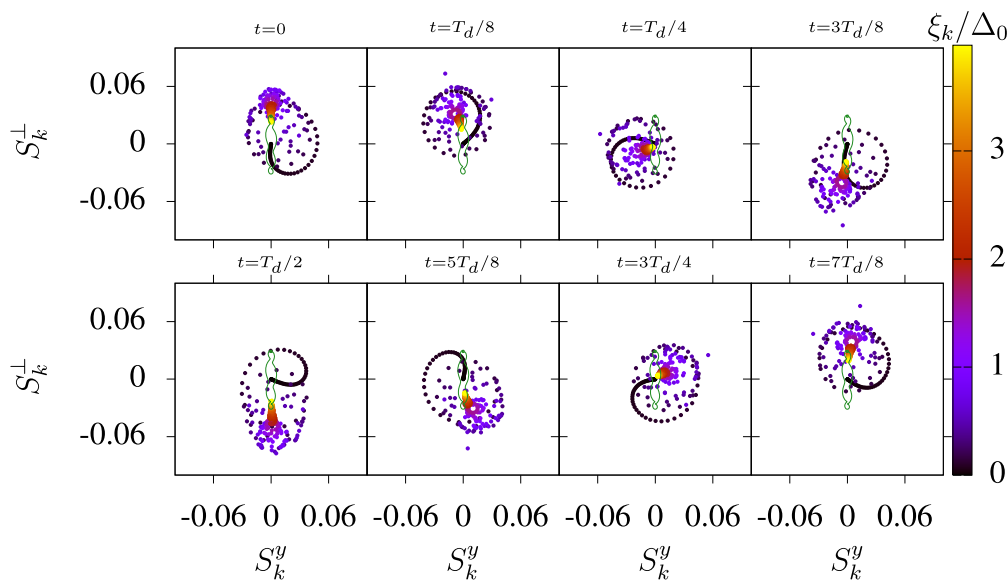


FIG. 6. We show snapshots, during a time window T_d , of pseudospin dynamics in the synchronized Higgs mode phase [$\alpha = 0.05$ and $\omega_d = 0.8\Delta_0$ corresponding with the parameters used in Figs. 2(a) and 2(b)]. At the top of the panels, we indicate the time. A pseudospin trajectory for $\xi_k \simeq 3\Delta_0$ is shown in green. See also the Supplemental Material [67] for a video of the dynamics.

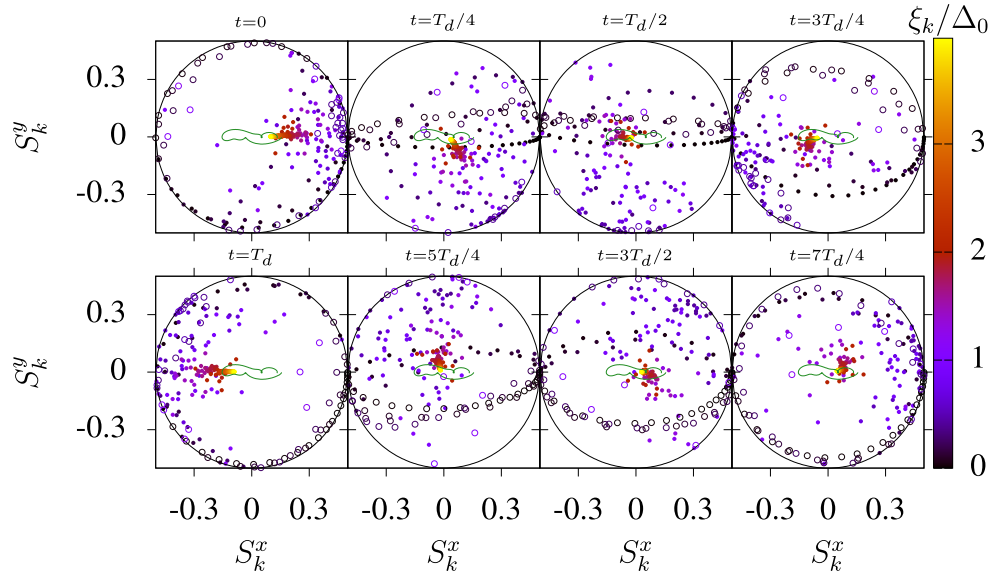


FIG. 7. Dynamics in the time-crystal phase. We show snapshots, during a time window $2T_d$, of pseudospin dynamics in the time-crystal phase. Here, $\alpha = 0.05$ and $\omega_d = 1.64\Delta_0$ corresponding with the parameters used in Figs. 2(c) and 2(d). At the top of the panels we indicate the time. The green loop points out a typical trajectory of pseudospins (orange dots). Those pseudospins with $S_k^z > 0$ ($S_k^z < 0$) are indicated with solid (open) dots. See also the Supplemental Material [67] for a video of the dynamics.

B. Discrete time-crystal phase

We now turn to the discrete time-crystal phase. Because $\bar{\Delta} = 0$ is very far from the equilibrium value Δ_0 , it is convenient to use a Cartesian frame instead of the ELF. Figure 7 shows the dynamics during a $2T_d$ time window. Solid (open) symbols indicate $S_k^z > 0$ ($S_k^z < 0$). The high-energy pseudospins (red-yellow dots) precess around the instantaneous pseudomagnetic field describing a loop (green line) and contributing self-consistently to build the time-dependent order parameter. Very-low-energy pseudospins have a nearly maximal component in the xy plane in the first frame, indicating strong pairing correlations but with incoherent phases. This initial circular feature becomes an ellipse at subsequent times, corresponding to a ring that rotates nearly rigidly along the x axis of the Bloch sphere. Spins at intermediate energies (violet-orange dots) interpolate between these two behaviors, contributing significantly to the time-dependent $\Delta(t)$. Indeed, the red and violet cloud is on the right-hand side of the frame at $t = 0$ contributing to a positive Δ [cf. Eq. (4)] and after one drive period has shifted to the left, yielding the sign alternation of Δ in one drive period as shown in Fig. 2(c). After two drive periods, the pattern goes approximately back to the original distribution, consistently with the behavior of the order parameter.

C. Rabi-Higgs phase

Turning now to the Rabi-Higgs phase, since the order parameter is close to equilibrium, it is convenient to use the ELF once again. In Fig. 8 we show several texture snapshots during the first Rabi-Higgs period T_{RH} . At $t = 0$ (equilibrium) the pseudospin texture corresponds to all pseudospins at the origin by definition. For $t = T_{RH}/2$ we have the inversion phenomenon in which a subset of pseudospins (open dots) get inverted with respect to its fermionic energy. In other

words, they have an instantaneous negative S_k^z while $\xi_k > 0$. Since the z component of the pseudospin encodes the charge, this corresponds to an inversion of the quasiparticle population. The pseudospins that get inverted satisfy the resonance condition $\omega_d = \omega_L(\xi_k^*)$ with $\omega_L(\xi_k) = 2\sqrt{\xi_k^2 + \Delta_0^2}$, the natural Larmor frequency. We indicate this fermionic energy ξ_k^* with a cross in the color bar. After one full Rabi period, this inversion gets largely diminished. In the steady state one observes a periodic oscillation of the population as discussed in Ref. [21].

D. Gapless phase

Finally, for the gapless phase it is convenient to go back to the Cartesian frame. In Fig. 9 we show texture snapshots at short times. We see that after a fast transient, the pseudospins start to roll up around the coordinate origin with the shape of a spiral. This unveils that the gapless phase consists in strong pairing correlations, i.e., for several pseudospins $S_k^x \neq 0$, but with Cooper pairs which are not phase coherent. So the sum of the x components yields a zero gap. This is not, however, a chaotic state, but the ZOPA is a consequence of a very orderly movement of pseudospins consistent with the unitary evolution of the state.

V. DYNAMICAL PHASE TRANSITIONS

In order to characterize the order of the different DPTs, we analyze the behavior of the system along the dashed vertical line in Fig. 1(a) corresponding to $\alpha = 0.05$. Figure 10(a) shows the FT of the time-dependent superconducting order parameter as a function of ω_d while Fig. 10(b) shows its long-term average in the steady state, $\bar{\Delta}$.

In the adiabatic limit ($\omega_d \ll 2\Delta_0$), the FT shows a clear peak at ω_d resulting in the strong linear orange feature

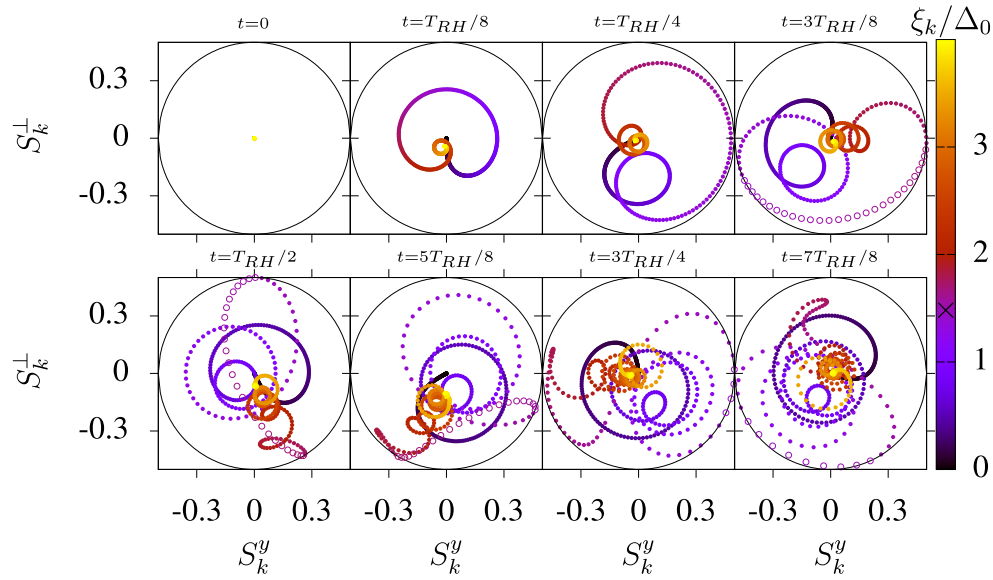


FIG. 8. Dynamics in the Rabi-Higgs phase. We show snapshots, during the first Rabi period T_{RH} , of pseudospin dynamics in the Rabi-Higgs regime [$\alpha = 0.12$ and $\omega_d = 3.5\Delta_0$ corresponding with the parameters used in Figs. 2(e) and 2(f)]. At the top of the panels, we indicate the time. Those pseudospins with $S_k^z > 0$ ($S_k^z < 0$) are indicated with solid (open) dots. The cross in the color bar indicates the ξ_k^* satisfying the resonance condition $\omega_L(\xi_k^*) = \omega_d$. See also the Supplemental Material [67] for a video of the dynamics.

in Fig. 10(a) as expected from linear response. A weaker feature appears at $2\omega_d$ corresponding to the allowed [23] second harmonic generation. Increasing ω_d , the dynamical order parameter $\bar{\Delta}$ [Fig. 10(b)] shows discontinuities near $\omega_d/(2\Delta_0) = 1/2$ and $\omega_d/(2\Delta_0) = 1/3$ corresponding to first-order DPTs associated to low- α precursors of the Arnold tongues [cf. Fig. 1(a)]. Inside the dynamical phases with finite $\bar{\Delta}$, well-defined peaks appear at ω_H and $\omega_H \pm \omega_d$ associated with the synchronized Higgs mode. The dotted lines in Fig. 10(a) are $2\bar{\Delta}$ (large dots) and $2\bar{\Delta} \pm \omega_d$ (small dots),

showing that the frequency of the Higgs mode is locked at $2\bar{\Delta}$. This can be seen as incommensurate time-crystal behavior similar to Ref. [24].

For $2\omega_d$ higher than the minimum of the effective continuum $2\bar{\Delta}$, the second harmonic of the drive is resonant with the quasiparticles. This produces a proliferation of excitations resulting in a suppression of the average gap as shown in Fig. 10(b) for $\omega_d/2\Delta_0 \approx 1/2$. As ω_d decreases, the $2\omega_d$ resonance approaches the quasiparticle minimum and the range of resonant quasiparticles gets cut off. At some point, there are

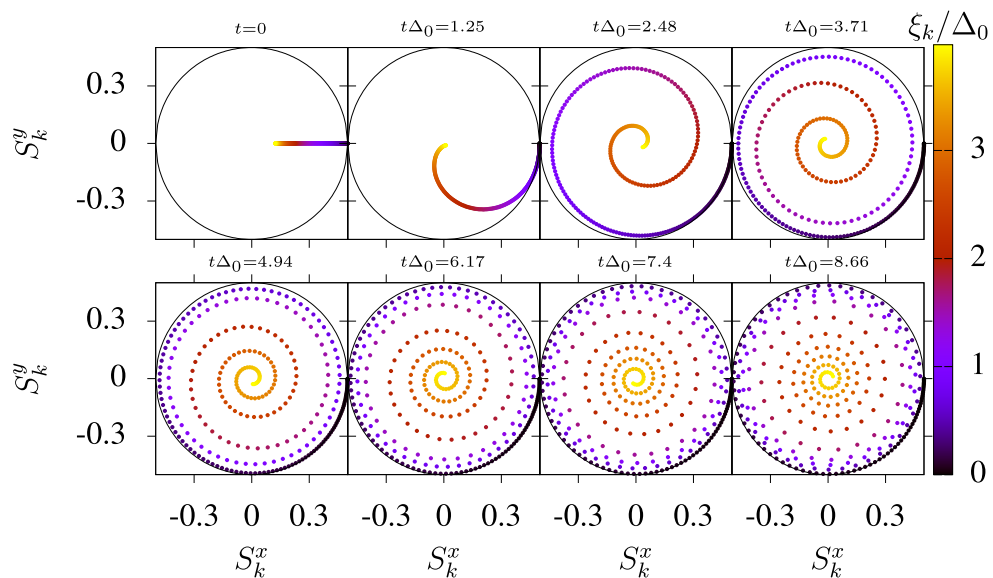


FIG. 9. Dynamics in the gapless regime. We show snapshots, during the transient to the gapless behavior, of pseudospin dynamics in the gapless phase [$\alpha = 0.27$ and $\omega_d = 3.5\Delta_0$ corresponding with the parameters used in Figs. 2(g) and 2(h)]. At the top of the panels, we indicate the time. See also the Supplemental Material [67] for a video of the dynamics.

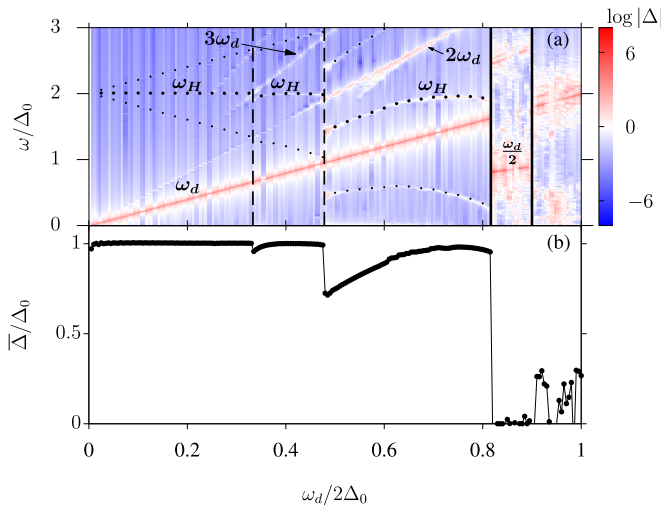


FIG. 10. (a) Characterization of DPTs through a false color plot of the superconducting response in the frequency domain vs driving frequency, ω_d for $\alpha = 0.05$. We used $t\Delta_0 \in [1500, 2500]$ for high-frequency resolution. Large and small dots represent $2\bar{\Delta}$ [shown also in (b)] and $2\bar{\Delta} \pm \omega_d$, respectively. These values are taken from the real time gap dynamics $\Delta(t)$. Notice that they match peaks in the FT. Vertical lines indicate equal symmetry (dashed) and different symmetry (solid) first-order DPTs. (b) Average of superconducting order parameter vs drive frequency.

not enough quasiparticles with $2\sqrt{\xi_k^2 + \bar{\Delta}^2} \approx 2\omega_d$ to suppress the gap and a new steady state is found, in which the Higgs mode frequency increases discontinuously with $\omega_H > 2\omega_d$. Thus, the line $\omega = 2\omega_d$ intersects the jump of ω_H in Fig. 10(a). A similar mechanism applies to the weaker transition at lower frequency, with the third harmonic resonance and the line $\omega = 3\omega_d$ intercepting the jump of ω_H .

While the previous two DPTs are among phases with the same symmetry, the third discontinuity at $\omega_d/2\Delta_0 \simeq 0.8$ represents a DPT between qualitatively distinct phases: gapped on the left and ZOPA on the right. The ZOPA phase corresponds to the $n = 1$ Arnold tongue and is bounded by the solid vertical lines in Fig. 11(a). Inside this region ($0.8 \lesssim \omega_d/2\Delta_0 \lesssim 0.9$), a commensurate time crystal appears with a doubling of the period of the drive. The persistence of the order parameter oscillation at $\omega_d/2$ in this finite region indicates that the period doubling is not accidental. As discussed in Ref. [27] this is also true changing α in a finite range. Thus, we confirm again that this state satisfies the rigidity criteria [58] for time-crystal behavior.

Both transitions bounding the time-crystal phase are first order. The upper edge of the tongue has a fractal-like appearance [27] which has been noticed also in related models [62]. Even inside the tongue, as already mentioned, marbled textures appear where $\bar{\Delta}$ becomes nonzero. In these cases, as illustrated in the rightmost part of Fig. 10(a), the time crystal is lost and the system switches to a phase in which time-translational symmetry is recovered at $\omega_d/2\Delta_0 \sim 0.9$ (marked with a second vertical line in the figure). For higher frequencies, the system enters a complex regime in which our numerical calculations show instabilities. In general, we

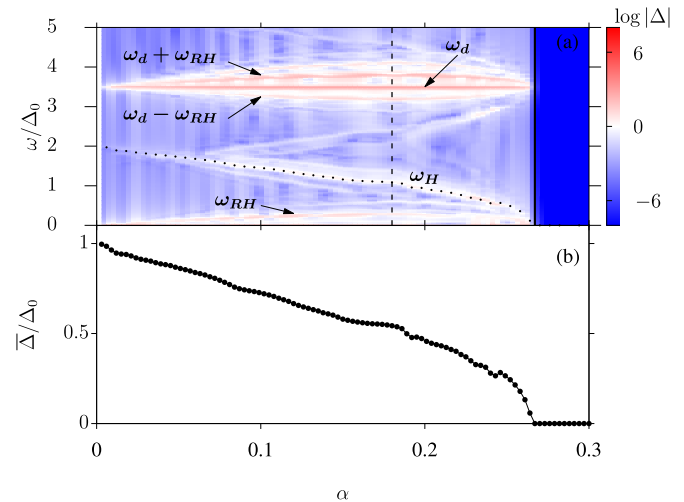


FIG. 11. (a) The superconducting response in the frequency domain vs the amplitude of the drive α for $\omega_d = 3.5\Delta_0$. We used $t\Delta_0 \in [10, 200]$ to compute the average and the FT. Small dots represent $2\bar{\Delta}$ [shown also in (b)]. These values are taken from the real time gap dynamics $\Delta(t)$ and match peaks in the FT. The dashed vertical line indicates the α value for which the Rabi-Higgs mode starts to soften. The solid vertical line instead points out the second-order DPTs to a gapless regime. The blue region on the right corresponds to $\Delta = 0$. (b) Average of superconducting order parameter vs drive amplitude.

find that when $\bar{\Delta} \simeq 0$ (for $\omega_d < 2\Delta_0$) a time-crystal phase emerges.

Now we discuss the DPTs along the horizontal dashed line $\omega_d = 3.5\Delta_0$ shown in Fig. 1(a). Figure 11(a) shows the FT map of $\Delta(t)$ for different values of the drive amplitude α . For extremely weak perturbation amplitudes, the system essentially responds with the drive frequency and the Higgs mode $\omega_H = 2\bar{\Delta}$ as occurs for drive frequencies below the gap. As soon as we increase the drive amplitude α , the Rabi-Higgs mode ω_{RH} appears in the spectrum, whose frequency increases linearly by increasing α . At the same time, satellites at frequencies $\omega_d \pm n\omega_{RH}$ with $n = 1, 2$ appear in the FT. Slightly less prominent, but still appreciable, are peaks at $\omega_H \pm \omega_{RH}$ witnessed by white branches near ω_H that linearly grow with α .

Increasing even more the amplitude, it is clear from Fig. 11(a) that there is a critical value α (marked by the vertical dashed line) in which the Rabi-Higgs mode starts to soften. It is more clearly seen in the satellite peaks $\omega_d \pm \omega_{RH}$. This is an *anomalous* behavior, taking into account that a conventional Rabi frequency increases by increasing the amplitude of the drive. Increasing even more the drive, the Rabi-Higgs and Higgs modes disappear and the system enters into a gapless regime [blue area in Fig. 11(a)]. In this case, not only $\bar{\Delta} = 0$ but also $\Delta = 0$ (i.e., the superconducting order parameter is zero over time without exhibiting oscillations). This DPT is indicated by a solid vertical line. In contrast to the first-order DPTs described in Fig. 10, here both the dynamics and the order parameter $\bar{\Delta}$, shown in Fig. 11(b), point to a second-order DPT with the characteristic “critical slowing down” near the transition point.

VI. MAPPING TO CLASSICAL DYNAMICS

In order to investigate the origin of the parametric resonances found numerically in Fig. 1 it is useful to map the BCS dynamics to classical anharmonic oscillators [68]. This can be done because the dynamics of pseudospins can be mapped to the dynamics of a collection of *classical* spins \mathbf{S}_k . Such a dynamic is governed by the Hamilton equations $\partial_t \mathbf{S}_k = \{\mathcal{H}, \mathbf{S}_k\}$ using the usual Poisson brackets $\{S_k^\mu, S_{k'}^\nu\} = -\varepsilon_{\mu\nu\eta} \delta_{k,k'} S_k^\eta$ for angular momenta where μ, ν, η represents the x, y, z component and $\varepsilon_{\mu\nu\eta}$ is the Levi-Civita tensor.

Alternatively one can derive the BCS time-dependent equations from a variational principle, requiring that the wave function has a BCS form at each instant of time and using the elements of the generalized one-particle density matrix as dynamical variables [53,68–71]. For each pair ($\mathbf{k} \uparrow, -\mathbf{k} \downarrow$), four expectation values of the one-particle density matrix need to be considered, corresponding to the four operators appearing on the right-hand side of Eqs. (2).

One can show that the density matrix derives from a BCS state if and only if the generalized matrix is idempotent [69]. It is easy to show that this is equivalent to the following constraints:

$$(S_k^x)^2 + (S_k^y)^2 + (S_k^z)^2 = 1/4, \quad (20)$$

$$\langle \hat{c}_{k\uparrow}^\dagger \hat{c}_{k\uparrow} \rangle = \langle \hat{c}_{-k\downarrow}^\dagger \hat{c}_{-k\downarrow} \rangle. \quad (21)$$

We can use Eq. (21) to reduce the dynamical variables for a pair ($\mathbf{k} \uparrow, -\mathbf{k} \downarrow$) to three variables which can then be taken as the pseudospin expectation values S_k^x, S_k^y, S_k^z with the constraint in Eq. (20).

In this formalism, the time-dependent expectation value of the quantum Hamiltonian plays the role of a classical Hamiltonian and can be obtained from Eq. (1) replacing operators by their expectation values in the instantaneous BCS wave function. Adding the constraint in Eq. (20) with Lagrange multipliers ω_k , the classical Hamiltonian reads

$$\begin{aligned} \mathcal{H} = & - \sum_k 2S_k^z \xi_k - \lambda \sum_{k,k'} (S_k^x S_{k'}^x + S_k^y S_{k'}^y) \\ & - 2f \sum_k S_k^x + \sum_k \omega_k \left[(S_k^x)^2 + (S_k^y)^2 + (S_k^z)^2 - \frac{1}{4} \right]. \end{aligned} \quad (22)$$

The third term is an additional external pairing field which couples linearly with the order parameter and which we added for later use. As before, driving will be introduced by making ξ_k, λ , or f time dependent. Here we concentrate on the λ driving and discuss briefly f driving. The DOS-driving protocol can be treated similarly.

It is useful to use as dynamical variables the deviation (not necessarily small) δS_k^μ defined as $S_k^\mu \equiv S_k^{\mu,0} + \delta S_k^\mu$, with $S_k^{\mu,0}$ the equilibrium BCS state. We also write the time dependence of the pairing interaction as an average value λ_0 plus a fluctuation, $\lambda = \lambda_0 + \delta\lambda$. The Hamiltonian can be written as $\mathcal{H} = E_0 + \delta\mathcal{H}$ with E_0 the equilibrium BCS ground-state

energy and with the fluctuating part,

$$\begin{aligned} \delta\mathcal{H} = & -2 \sum_k \delta S_k^z \xi_k - \delta\lambda \sum_{k,k'} (S_k^{x,0} S_{k'}^{x,0} + S_k^{y,0} S_{k'}^{y,0}) \\ & - 2(\lambda_0 + \delta\lambda) \sum_{k,k'} (\delta S_k^x S_{k'}^{x,0} + \delta S_k^y S_{k'}^{y,0}) \\ & - (\lambda_0 + \delta\lambda) \sum_{k,k'} (\delta S_k^x \delta S_{k'}^x + \delta S_k^y \delta S_{k'}^y) \\ & + \sum_k \omega_k [2S_k^{x,0} \delta S_k^x + 2S_k^{y,0} \delta S_k^y + 2S_k^{z,0} \delta S_k^z \\ & + (\delta S_k^x)^2 + (\delta S_k^y)^2 + (\delta S_k^z)^2] - 2f \sum_k \delta S_k^x. \end{aligned} \quad (23)$$

The saddle-point condition requires that linear variations vanish, which, by setting $f = \delta\lambda = 0$, yields the equilibrium mean-field equations

$$-\Delta_0^x + \omega_k S_k^{x,0} = 0, \quad (24)$$

$$-\Delta_0^y + \omega_k S_k^{y,0} = 0, \quad (25)$$

$$-\xi_k + \omega_k S_k^{z,0} = 0, \quad (26)$$

with $\Delta_0^\mu = \lambda_0 \sum_k S_k^{\mu,0}$ which can be readily solved for $S_k^{\mu,0}$. Without loss of generality, we take $\Delta_0^x = \Delta_0$ and $\Delta_0^y = 0$. Applying the constraint to the stationary state, one finds that the Lagrange multiplier is given by the equilibrium Larmor frequency, $\omega_k = \omega_L(\xi_k) = 2\sqrt{\xi_k^2 + \Delta_0^2}$. The negative root can be discarded as it yields the unphysical sign of $S_k^{z,0}$. Solving for the spin components yields Eq. (6).

Using the saddle-point condition, the Hamiltonian has terms up to cubic in fluctuations and is given by

$$\begin{aligned} \delta\mathcal{H} = & -(\lambda_0 + \delta\lambda) \sum_{k,k'} (\delta S_k^x \delta S_{k'}^x + \delta S_k^y \delta S_{k'}^y) \\ & + \sum_k \omega_k [(\delta S_k^x)^2 + (\delta S_k^y)^2 + (\delta S_k^z)^2] \\ & - 2 \left(\frac{\delta\lambda}{\lambda_0} \Delta_0 + f \right) \sum_k \delta S_k^x, \end{aligned} \quad (27)$$

where we dropped terms linear in $\delta\lambda$ which do not affect the EOM. It is useful to transform the Hamiltonian to the ELF of Eq. (19) to obtain

$$\begin{aligned} \delta\mathcal{H} = & \sum_k \omega_k [(\delta S_k^y)^2 + (\delta S_k^\perp)^2 + (\delta S_k^\parallel)^2] \\ & - (\lambda_0 + \delta\lambda) \sum_{k,k'} \left(4 \frac{\xi_k \xi_{k'}}{\omega_k \omega_{k'}} \delta S_k^\perp \delta S_{k'}^\perp + \delta S_k^y \delta S_{k'}^y \right) \\ & - 4 \left(\frac{\delta\lambda}{\lambda_0} \Delta_0 + f \right) \sum_k \frac{\xi_k}{\omega_k} \delta S_k^\perp. \end{aligned} \quad (28)$$

A. Harmonic approximation

So far, the treatment is exact. We now proceed by introducing some approximations. First, one can use the constraint to show that longitudinal fluctuations are higher order compared to transverse ones (which can be also seen from a geometric

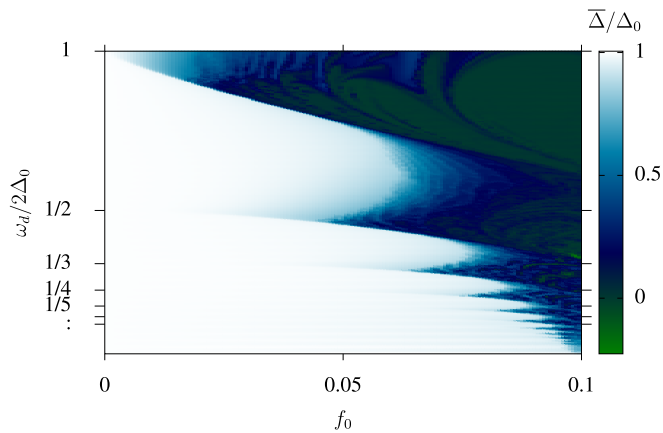


FIG. 12. Dynamical phase diagram for periodic driving by an external pairing field. We show the temporal average of the superconducting order parameter in the $f_0 - \omega_d$ plane for the case of an external pairing field drive.

argument). Thus, we neglect δS_k^{\parallel} in the first term of Eq. (28). Defining canonical variables as $p_k = \sqrt{2}\delta S_k^y$ and $q_k = \sqrt{2}\delta S_k^x$ the energy reads

$$\begin{aligned} \delta\mathcal{H} = & \frac{1}{2} \sum_k \omega_k (p_k^2 + q_k^2) \\ & - (\lambda_0 + \delta\lambda) \sum_{k,k'} \left(2 \frac{\xi_k \xi_{k'}}{\omega_k \omega_{k'}} q_k q_{k'} + \frac{1}{2} p_k p_{k'} \right) \\ & - 2\sqrt{2} \left(\frac{\delta\lambda}{\lambda_0} \Delta_0 + f \right) \sum_k \frac{\xi_k}{\omega_k} q_k, \end{aligned} \quad (29)$$

which maps the problem to a set of harmonic oscillators with long-range interactions depending on the quasiparticle energy ξ_k . The Larmor frequency $\omega_L(\xi_k)$ plays the role of natural frequencies of the oscillators, giving rise to a DOS in frequency space peaking at $2\Delta_0$, consistent with the identification of $\omega_0 = 2\Delta_0$ as the ‘‘natural frequency’’ of oscillation of the superconducting system [27].

Setting $f = 0$, one can check that the Hamilton EOM,

$$\dot{q}_k = \frac{\partial \mathcal{H}}{\partial p_k}, \quad \dot{p}_k = -\frac{\partial \mathcal{H}}{\partial q_k}, \quad (30)$$

reproduce the linearized version of Eq. (7).

Fluctuations in λ couple linearly with the canonical variables [last term in Eq. (29)] and with quadratic fluctuations of canonical variables (second term). In analogy with a single classical parametric oscillator [64], it is tempting to attribute parametric resonances to the coupling with quadratic fluctuations. However, this can be excluded in the following way. We set $\delta\lambda = 0$ and consider periodic driving in $f = f_0 \sin(\omega_d t)$. From Eq. (29), we see that this driving is equivalent to the linear coupling with $\delta\lambda$ (for that term). Figure 12 shows the phase diagram computed with the *original* Hamiltonian, Eq. (22), but with f as the only time-dependent perturbation. In this case, one obtains similar Arnold tongues which reveals that the coupling of $\delta\lambda$ with quadratic fluctuations is not essential to obtain the parametric resonances. This result could be anticipated from the following argument. Since quadratic

fluctuations of canonical variables couple linearly with $\delta\lambda$ [cf. Eq. (29)], the analogy with a single parametric oscillator would yield parametric resonances at $\omega_d = 2\omega_0/n = 4\Delta_0/n$ which is not consistent with the resonances obtained numerically [Fig. 1(a)], which satisfy instead $\omega_d = \omega_0/n = 2\Delta_0/n$.

We will see that the linear coupling of $\delta\lambda$ with canonical variables [last term in Eq. (29)] plays a fundamental role in the emergence of the parametric resonances. This does not occur through the direct coupling with the pseudospin fluctuations but indirectly through the effect of higher-order nonlinearities.

B. Higher orders

Writing the constraint on the pseudospin length as $2\mathbf{S}_k^0 \cdot \delta\mathbf{S}_k + |\delta\mathbf{S}_k|^2 = \delta S_k^{\parallel} + |\delta\mathbf{S}_k|^2 = 0$, we can eliminate longitudinal fluctuations in favor of transverse ones,

$$\frac{1}{2} + \delta S_k^{\parallel} = \pm \frac{1}{2} \sqrt{1 - 4(\delta S_k^y)^2 + (\delta S_k^x)^2}, \quad (31)$$

where the left-hand side is nothing but S_k^{\parallel} . We see that for the solution to be real $(\delta S_k^y)^2 + (\delta S_k^x)^2 < 1/4$ and two solutions are possible, one in which $S_k^{\parallel} > 0$ (ferroalignment) and one in which $S_k^{\parallel} < 0$ (antiferroalignment). Although both solutions are needed for the full dynamics, for the time being we restrict to ferroalignment which is the relevant solution for not too large deviations.

Considering only the λ driving and using canonical variables q_k and p_k , the Hamiltonian reads

$$\begin{aligned} \delta\mathcal{H} = & \sum_k \frac{\omega_k}{2} (1 - \sqrt{1 - 2(p_k^2 + q_k^2)}) \\ & - (\lambda_0 + \delta\lambda) \sum_{k,k'} \left(2 \frac{\xi_k \xi_{k'}}{\omega_k \omega_{k'}} q_k q_{k'} + \frac{1}{2} p_k p_{k'} \right) \\ & - 2\sqrt{2} \frac{\delta\lambda}{\lambda_0} \Delta_0 \sum_k \frac{\xi_k}{\omega_k} q_k, \end{aligned} \quad (32)$$

where again one can check that Hamilton equations yield the correct EOM.

Expanding the square root in a Taylor series, the first term in Eq. (32) can be written as a collection of anharmonic oscillators, $\sum_k \frac{\Omega_k}{2} (p_k^2 + q_k^2)$, with a time-dependent self-consistently determined natural frequency,

$$\begin{aligned} \Omega_k(t) = & \omega_k \left[1 + \frac{1}{2} (p_k^2 + q_k^2) + \frac{1}{2} (p_k^2 + q_k^2)^2 \right. \\ & \left. + \frac{5}{8} (p_k^2 + q_k^2)^3 + \dots \right]. \end{aligned} \quad (33)$$

Following Ref. [64] we can analyze nonlinearities iteratively. Treating the last term in Eq. (32) in linear response [21] one obtains that for a drive frequency ω_d , the quadratic terms respond as $(p_k^2 + q_k^2) \propto \cos 2\omega_d t$ which implies that the natural frequency Ω_k is ‘‘pumped’’ with frequency $\omega_p = 2\omega_d$. Thus, using the fact that a classical oscillator has parametric resonances at $\omega_d = 2\omega_0/n$, one expects resonances at $\omega_d = 2\Delta_0/n$ in the BCS system, as indeed found. The identification of the pump mechanism and the explanation of the factor of 2 in the resonance series is the main result of this section. We remark that this ingredient alone is not enough to explain the parametric resonances. Indeed, the nonlinear effects described

arise from the constraint while in Sec. III we showed that interactions, represented here by the second line in Eq. (32), are essential to stabilize parametric resonances. Furthermore, restricting to the “ferro” alignment root in Eq. (32) is not enough in the parametric resonance regime as numerically we find that the dynamics explore both roots (see Fig. 7). On the other hand, these considerations do not affect the conclusion that the leading pump frequency for the oscillators is at $\omega_p = 2\omega_d$ instead of ω_d as adding more nonlinearities can only produce higher multiples of ω_d .

VII. SUMMARY AND CONCLUSIONS

We have presented a comprehensive dynamical phase diagram for a periodically driven BCS condensate using different driving protocols. We concentrated on superconducting and/or superfluid phases but our results are valid for any phase for which a BCS description is valid in the time regime before energy relaxation processes take place in the system. This includes weak-coupling spin and charge density waves which can also be mapped to the BCS model.

We numerically demonstrated that the existence of four dynamical phases and parametric resonances are quite robust to changes in the protocol. To a large extent, the phase diagram can be said to be universal. We expect the main features to remain, also, for more complicated drives, which for example may be anisotropic on the Fermi surface and depend on light polarization acting as the drive.

A detailed analysis of the evolution of the pseudospin textures (Figs. 6–9) allowed to visualize how the many-body system spontaneously self-organizes in momentum space in sectors with different dynamics. For the gapless phase, our analysis revealed a remarkable degree of order and symmetry in this, apparently, unbroken symmetry phase.

Our study allowed to identify the order of the phase transitions. Roughly speaking, parametric resonances at $2\Delta_0/n$ can be seen as multiphoton process with n photons reaching the gap. Continuous excitation produces a depletion of the gap which lowers the threshold for excitation. This provides a feedback loop that explains the first-order transitions in the lower edge of the Arnold tongues. Second-order phase transitions also arise by increasing the intensity of the drive from the Rabi-Higgs to the gapless phase. This is accompa-

nied by a critical slowing down of the dynamics. Thus, the Rabi-Higgs frequency first follows the common expectation for a Rabi mode; its frequency increases with drive strength. For large driving strength it switches to an anomalous regime in which its frequency decreases with strength.

For subgap excitations, by combining different driving protocols and mapping to a system of nonlinear oscillators, we showed that the mechanism of the parametric pump can be traced back to the nonlinearity in the system due to the constraint on the length of pseudospins. Furthermore, we demonstrated that to take into account interactions self-consistently is an essential ingredient to obtain parametric resonances. In other words, they constitute an emergent phenomenon of the many-body system.

Regarding experimental realizations, while the present model neglects the presence of a bath, we have previously shown that parametric resonances and time-crystal behavior appear at very early times in the dynamics [27]. In the presence of a finite decoherence time, they may be observed as a prethermal transient in the dynamics. Proposed realizations in the solid state include terahertz excitations and a phonon-assisted λ -driving mechanism [21]. Ultracold atoms are also very interesting platforms which are inherently much less affected by the environment (lattice vibrations are not present). Furthermore, they offer a large degree of parameter manipulation, making them ideal candidates to study the driven BCS system [6]. Yet another promising platform to observe the present phenomena is a cavity-QED simulator, where Anderson’s pseudospin model can be directly studied [10]. Our work is an invitation to exploit these platforms to experimentally explore the fascinating time-translational-symmetry-breaking phases of periodically driven BCS systems.

ACKNOWLEDGMENTS

We acknowledge financial support from ANPCyT (Grants No. PICT 2016-0791, No. PICT 2018-1509, and No. PICT 2019-0371), CONICET (Grant No. PIP 11220150100506), SeCyT-UNCuyo (Grant No. 06/C603), and the Italian Ministry for University and Research through PRIN Projects No. 2017Z8TS5B and No. 20207ZXT4Z. H.P.O.C. is supported by the Marie Skłodowska-Curie individual fellowship Grant Agreement No. SUPERDYN 893743.

-
- [1] T. Oka and S. Kitamura, Floquet engineering of quantum materials, *Annu. Rev. Condens. Matter Phys.* **10**, 387 (2019).
 - [2] M. Bukov, L. D’Alessio, and A. Polkovnikov, Universal high-frequency behavior of periodically driven systems: From dynamical stabilization to Floquet engineering, *Adv. Phys.* **64**, 139 (2015).
 - [3] P. W. Claeys, M. Pandey, D. Sels, and A. Polkovnikov, Floquet-Engineering Counterdiabatic Protocols in Quantum Many-Body Systems, *Phys. Rev. Lett.* **123**, 090602 (2019).
 - [4] F. Meinert, M. J. Mark, K. Lauber, A. J. Daley, and H.-C. Nägerl, Floquet Engineering of Correlated Tunneling in the Bose-Hubbard Model with Ultracold Atoms, *Phys. Rev. Lett.* **116**, 205301 (2016).
 - [5] J. Eisert, M. Friesdorf, and C. Gogolin, Quantum many-body systems out of equilibrium, *Nat. Phys.* **11**, 124 (2015).
 - [6] A. Behrle, T. Harrison, J. Kombe, K. Gao, M. Link, J.-S. Bernier, C. Kollath, and M. Köhl, Higgs mode in a strongly interacting fermionic superfluid, *Nat. Phys.* **14**, 781 (2018).
 - [7] C. Chin, R. Grimm, P. Julienne, and E. Tiesinga, Feshbach resonances in ultracold gases, *Rev. Mod. Phys.* **82**, 1225 (2010).
 - [8] A. Eckardt, Colloquium: Atomic quantum gases in periodically driven optical lattices, *Rev. Mod. Phys.* **89**, 011004 (2017).
 - [9] J. A. Muniz, D. Barberena, R. J. Lewis-Swan, D. J. Young, J. R. K. Cline, A. M. Rey, and J. K. Thompson, Exploring dynamical phase transitions with cold atoms in an optical cavity, *Nature (London)* **580**, 602 (2020).

- [10] R. J. Lewis-Swan, D. Barberena, J. R. K. Cline, D. J. Young, J. K. Thompson, and A. M. Rey, Cavity-QED Quantum Simulator of Dynamical Phases of a Bardeen-Cooper-Schrieffer Superconductor, *Phys. Rev. Lett.* **126**, 173601 (2021).
- [11] M. A. Norcia, R. J. Lewis-Swan, J. R. K. Cline, B. Zhu, A. M. Rey, and J. K. Thompson, Cavity-mediated collective spin-exchange interactions in a strontium superradiant laser, *Science* **361**, 259 (2018).
- [12] J. Zhang, G. Pagano, P. W. Hess, A. Kyprianidis, P. Becker, H. Kaplan, A. V. Gorshkov, Z. X. Gong, and C. Monroe, Observation of a many-body dynamical phase transition with a 53-qubit quantum simulator, *Nature (London)* **551**, 601 (2017).
- [13] F. Görg, M. Messer, K. Sandholzer, G. Jotzu, R. Desbuquois, and T. Esslinger, Enhancement and sign change of magnetic correlations in a driven quantum many-body system, *Nature (London)* **553**, 481 (2018).
- [14] J. W. McIver, B. Schulte, F.-U. Stein, T. Matsuyama, G. Jotzu, G. Meier, and A. Cavalleri, Light-induced anomalous Hall effect in graphene, *Nat. Phys.* **16**, 38 (2019).
- [15] S. Borroni, E. Baldini, V. M. Katukuri, A. Mann, K. Parlinski, D. Legut, C. Arrell, F. van Mourik, J. Teyssier, A. Kozłowski, P. Piekarczyk, O. V. Yazyev, A. M. Oleś, J. Lorenzana, F. Carbone, Coherent generation of symmetry-forbidden phonons by light-induced electron-phonon interactions in magnetite, *Phys. Rev. B* **96**, 104308 (2017).
- [16] D. Fausti, R. I. Tobey, N. Dean, S. Kaiser, A. Dienst, M. C. Hoffmann, S. Pyon, T. Takayama, H. Takagi, and A. Cavalleri, Light-induced superconductivity in a stripe-ordered cuprate, *Science* **331**, 189 (2011).
- [17] M. Mitrano, A. Cantaluppi, D. Nicoletti, S. Kaiser, A. Perucchi, S. Lupi, P. Di Pietro, D. Pontiroli, M. Riccò, S. R. Clark, D. Jaksch, and A. Cavalleri, Possible light-induced superconductivity in K_3C_{60} at high temperature, *Nature (London)* **530**, 461 (2016).
- [18] E. T. Mannila, P. Samuelsson, S. Simbierowicz, J. T. Peltonen, V. Vesterinen, L. Grönberg, J. Hassel, V. F. Maisi, and J. P. Pekola, A superconductor free of quasiparticles for seconds, *Nat. Phys.* **18**, 145 (2022).
- [19] G. Catelani and J. P. Pekola, Using materials for quasiparticle engineering, *Mater. Quantum Technol.* **2**, 013001 (2022).
- [20] O. P. Saira, A. Kemppinen, V. F. Maisi, and J. P. Pekola, Vanishing quasiparticle density in a hybrid Al/Cu/Al single-electron transistor, *Phys. Rev. B* **85**, 012504 (2012).
- [21] H. P. Ojeda Collado, J. Lorenzana, G. Usaj, and C. A. Balseiro, Population inversion and dynamical phase transitions in a driven superconductor, *Phys. Rev. B* **98**, 214519 (2018).
- [22] M. Claassen, D. M. Kennes, M. Zingl, M. A. Sentef, and A. Rubio, Universal optical control of chiral superconductors and Majorana modes, *Nat. Phys.* **15**, 766 (2019).
- [23] H. P. Ojeda Collado, G. Usaj, J. Lorenzana, and C. A. Balseiro, Nonlinear dynamics of driven superconductors with dissipation, *Phys. Rev. B* **101**, 054502 (2020).
- [24] G. Homann, J. G. Cosme, and L. Mathey, Higgs time crystal in a high- T_c superconductor, *Phys. Rev. Res.* **2**, 043214 (2020).
- [25] J.-A. Yang, N. Pellatz, T. Wolf, R. Nandkishore, and D. Reznik, Ultrafast magnetic dynamics in insulating $YBa_2Cu_3O_{6.1}$ revealed by time resolved two-magnon Raman scattering, *Nat. Commun.* **11**, 2548 (2020).
- [26] Q. Yang, Z. Yang, and D. E. Liu, Intrinsic dissipative Floquet superconductors beyond mean-field theory, *Phys. Rev. B* **104**, 014512 (2021).
- [27] H. P. Ojeda Collado, G. Usaj, C. A. Balseiro, D. H. Zanette, and J. Lorenzana, Emergent parametric resonances and time-crystal phases in driven Bardeen-Cooper-Schrieffer systems, *Phys. Rev. Res.* **3**, L042023 (2021).
- [28] R. Peña, V. M. Bastidas, F. Torres, W. J. Munro, and G. Romero, Fractional resonances and prethermal states in Floquet systems, *Phys. Rev. B* **106**, 064307 (2022).
- [29] R. Peña, T. H. Kyaw, and G. Romero, Stable many-body resonances in open quantum systems, *Symmetry* **14**, 2562 (2022).
- [30] M. Natsheh, A. Gambassi, and A. Mitra, Critical properties of the Floquet time crystal within the Gaussian approximation, *Phys. Rev. B* **103**, 014305 (2021).
- [31] M. Natsheh, A. Gambassi, and A. Mitra, Critical properties of the prethermal Floquet time crystal, *Phys. Rev. B* **103**, 224311 (2021).
- [32] D. V. Else, C. Monroe, C. Nayak, and N. Y. Yao, Discrete time crystals, *Annu. Rev. Condens. Matter Phys.* **11**, 467 (2020).
- [33] A. Lazarides, S. Roy, F. Piazza, and R. Moessner, Time crystallinity in dissipative Floquet systems, *Phys. Rev. Res.* **2**, 022002(R) (2020).
- [34] M. A. Sentef, A. Tokuno, A. Georges, and C. Kollath, Theory of Laser-Controlled Competing Superconducting and Charge Orders, *Phys. Rev. Lett.* **118**, 087002 (2017).
- [35] D. M. Kennes, M. Claassen, M. A. Sentef, and C. Karrasch, Light-induced d -wave superconductivity through Floquet-engineered Fermi surfaces in cuprates, *Phys. Rev. B* **100**, 075115 (2019).
- [36] H. P. Ojeda Collado, G. Usaj, J. Lorenzana, and C. A. Balseiro, Fate of dynamical phases of a BCS superconductor beyond the dissipationless regime, *Phys. Rev. B* **99**, 174509 (2019).
- [37] A. de la Torre, D. M. Kennes, M. Claassen, S. Gerber, J. W. McIver, and M. A. Sentef, Nonthermal pathways to ultrafast control in quantum materials, *Rev. Mod. Phys.* **93**, 041002 (2021).
- [38] M. Buzzi, D. Nicoletti, M. Fechner, N. Tancogne-Dejean, M. A. Sentef, A. Georges, T. Biesner, E. Uykur, M. Dressel, A. Henderson, T. Siegrist, J. A. Schlueter, K. Miyagawa, K. Kanoda, M. S. Nam, A. Ardavan, J. Coulthard, J. Tindall, F. Schlawin, D. Jaksch *et al.*, Photomolecular High-Temperature Superconductivity, *Phys. Rev. X* **10**, 031028 (2020).
- [39] M. Puviani, R. Haenel, and D. Manske, Transient excitation of Higgs and high-harmonic generation in superconductors with quench-drive spectroscopy, [arXiv:2112.12123](https://arxiv.org/abs/2112.12123).
- [40] G. Lyu, K.-T. Xi, S. Yoon, Q. Chen, and G. Watanabe, Exciting long-lived Higgs mode in superfluid Fermi gases with particle removal, [arXiv:2210.09829](https://arxiv.org/abs/2210.09829).
- [41] P. W. Anderson, Random-phase approximation in the theory of superconductivity, *Phys. Rev.* **112**, 1900 (1958).
- [42] R. A. Barankov, L. S. Levitov, and B. Z. Spivak, Collective Rabi Oscillations and Solitons in a Time-Dependent BCS Pairing Problem, *Phys. Rev. Lett.* **93**, 160401 (2004).
- [43] E. A. Yuzbashyan, B. L. Altshuler, V. B. Kuznetsov, and V. Z. Enolskii, Solution for the dynamics of the BCS and central spin problems, *J. Phys. A: Math. Gen.* **38**, 7831 (2005).

- [44] E. A. Yuzbashyan, B. L. Altshuler, V. B. Kuznetsov, and V. Z. Enolskii, Nonequilibrium Cooper pairing in the nonadiabatic regime, *Phys. Rev. B* **72**, 220503(R) (2005).
- [45] R. A. Barankov and L. S. Levitov, Dynamical selection in developing fermionic pairing, *Phys. Rev. A* **73**, 033614 (2006).
- [46] R. A. Barankov and L. S. Levitov, Synchronization in the BCS Pairing Dynamics as a Critical Phenomenon, *Phys. Rev. Lett.* **96**, 230403 (2006).
- [47] E. A. Yuzbashyan, O. Tsypliyatyev, and B. L. Altshuler, Relaxation and Persistent Oscillations of the Order Parameter in Fermionic Condensates, *Phys. Rev. Lett.* **96**, 097005 (2006).
- [48] E. A. Yuzbashyan and M. Dzero, Dynamical Vanishing of the Order Parameter in a Fermionic Condensate, *Phys. Rev. Lett.* **96**, 230404 (2006).
- [49] Y.-Z. Chou, Y. Liao, and M. S. Foster, Twisting Anderson pseudospins with light: Quench dynamics in terahertz-pumped BCS superconductors, *Phys. Rev. B* **95**, 104507 (2017).
- [50] S. Hannibal, P. Kettmann, M. D. Croitoru, A. Vagov, V. M. Axt, and T. Kuhn, Quench dynamics of an ultracold Fermi gas in the BCS regime: Spectral properties and confinement-induced breakdown of the Higgs mode, *Phys. Rev. A* **91**, 043630 (2015).
- [51] E. A. Yuzbashyan, M. Dzero, V. Gurarie, and M. S. Foster, Quantum quench phase diagrams of an *s*-wave BCS-BEC condensate, *Phys. Rev. A* **91**, 033628 (2015).
- [52] J. A. Scaramazza, P. Smacchia, and E. A. Yuzbashyan, Consequences of integrability breaking in quench dynamics of pairing Hamiltonians, *Phys. Rev. B* **99**, 054520 (2019).
- [53] G. Seibold, C. Castellani, and J. Lorenzana, Adiabatic transition from a BCS superconductor to a Fermi liquid and phase dynamics, *Phys. Rev. B* **105**, 184513 (2022).
- [54] H. P. Ojeda Collado, N. Defenu, and J. Lorenzana, Engineering Higgs dynamics by spectral singularities, [arXiv:2205.06826](https://arxiv.org/abs/2205.06826).
- [55] A. F. Volkov and Sh. M. Kogan, Collisionless relaxation of the energy gap in superconductors, *Zh. Eksp. Teor. Fiz* **65**, 2038 (1973).
- [56] T. Cea and L. Benfatto, Nature and Raman signatures of the Higgs amplitude mode in the coexisting superconducting and charge-density-wave state, *Phys. Rev. B* **90**, 224515 (2014).
- [57] D. V. Else, B. Bauer, and C. Nayak, Floquet Time Crystals, *Phys. Rev. Lett.* **117**, 090402 (2016).
- [58] N. Y. Yao, A. C. Potter, I.-D. Potirniche, and A. Vishwanath, Discrete Time Crystals: Rigidity, Criticality, and Realizations, *Phys. Rev. Lett.* **118**, 030401 (2017).
- [59] A. Russomanno, F. Iemini, M. Dalmonte, and R. Fazio, Floquet time crystal in the Lipkin-Meshkov-Glick model, *Phys. Rev. B* **95**, 214307 (2017).
- [60] J. Rovny, R. L. Blum, and S. E. Barrett, Observation of Discrete-Time-Crystal Signatures in an Ordered Dipolar Many-Body System, *Phys. Rev. Lett.* **120**, 180603 (2018).
- [61] N. Y. Yao, C. Nayak, L. Balents, and M. P. Zaletel, Classical discrete time crystals, *Nat. Phys.* **16**, 438 (2020).
- [62] G. Giachetti, A. Solfanelli, L. Correale, and N. Defenu, High-order time crystal phases and their fractal nature, [arXiv:2203.16562](https://arxiv.org/abs/2203.16562).
- [63] M. H. Muñoz-Arias, K. Chinni, and P. M. Poggi, Floquet time crystals in driven spin systems with all-to-all *p*-body interactions, *Phys. Rev. Res.* **4**, 023018 (2022).
- [64] L. D. Landau and E. M. Lifshitz, *Mechanics: Volume 1*, Course of Theoretical Physics (Butterworth-Heinemann, Oxford, UK, 1976).
- [65] T. L. Heugel, M. Oscity, A. Eichler, O. Zilberberg, and R. Chitra, Classical Many-Body Time Crystals, *Phys. Rev. Lett.* **123**, 124301 (2019).
- [66] Z. G. Nicolaou and A. E. Motter, Anharmonic classical time crystals: A coresonance pattern formation mechanism, *Phys. Rev. Res.* **3**, 023106 (2021).
- [67] See Supplemental Material at [<http://link.aps.org/supplemental/10.1103/PhysRevResearch.5.023014>] for a video of the pseudospin dynamics.
- [68] B. Sciolla and G. Biroli, Dynamical transitions and quantum quenches in mean-field models, *J. Stat. Mech. Theory Exp.* (2011) P11003.
- [69] J. P. Blaizot and G. Ripka, *Quantum Theory of Finite Systems* (MIT Press, Cambridge, MA, 1986).
- [70] M. Schiró and M. Fabrizio, Time-Dependent Mean Field Theory for Quench Dynamics in Correlated Electron Systems, *Phys. Rev. Lett.* **105**, 076401 (2010).
- [71] J. Bünamann, M. Capone, J. Lorenzana, and G. Seibold, Linear-response dynamics from the time-dependent Gutzwiller approximation, *New J. Phys.* **15**, 053050 (2013).